FULL PAPER

Probing the Photovoltage and Photocurrent in Perovskite Solar Cells with Nanoscale Resolution

Zhenxuan Zhao, Xiangyu Chen,* Huaqiang Wu, Xiaoming Wu, and Guozhong Cao*

In this work, by coupling scanning Kelvin probe force microscopy (SKPM) and photoconductive atomic force microscopy (pcAFM), the variation of the surface potential, photogenerated voltage, and photocurrent networks of the perovskite solar cells (PSCs) with different film topography is studied. The nanoscale photovoltaic reaction of different perovskite capping layers with three different perovskite crystalline sizes is first studied by using the SKPM technique. The performance of the overall device is correlated with the local nanostructure of the perovskite film. Photocurrent maps under various applied voltages are also presented. The pcAFM measurements on three different morphology positions determine that the defect region on the capping layer can induce the charge recombination process in the complete PSCs and thus suppress the V_{oc} in the complete device. These results suggest that the performance of PSCs can still be improved through better control of morphology. Henceforth, SKPM coupled with pcAFM techniques has the potential to become a routine characterization tool for perovskite organic and hybrid photovoltaics.

1. Introduction

Over the past few years, hybrid organic–inorganic perovskite solar cells (PSCs) have attracted tremendous attention as one of the most promising photovoltaic technologies and the power conversion efficiency (PCE) of these PCSs has experienced a series of breakthroughs with a certified value of over 17%.[1,2] It is based on organic–inorganic light absorbing semiconductor material with a perovskite polycrystalline structure, $CH_3NH_3PbX_3$, where X is a halide atom (I, Cl, Br, or a combination of some of them).

During the development of perovskite solar cell, many preparing methods, including solution processing and vapor-phase deposition,[3,4] have been invented. The solution processability is one of the major advantages of the PSCs, which requires only a simple heating step to build up crystalline perovskite form. Solution processing has many advantages, but equally has many limitations, such as uneven coverage of the perovskite capping layer, formation of pinholes, and relatively small grains in capping layer. All these limitations require more research and need to be addressed for high power conversion efficiency.[5] The morphology and crystallinity of the formed perovskite layer greatly determines the overall device performance. Previous reports have demonstrated the PCE of over 15% from a planar heterojunction perovskite solar cell,[3] which is attributed to the formation of extremely uniform flat film by vapor deposition. Since then, a great variety of works has been proposed to improve the PCEs of the devices by modifying their morphologies as well as deposition methodologies of the perovskite layer, such as sequential step procedures,[2] or employing different precursors for the film formation.[6] Moreover, the perovskite crystallization requires an appropriate temperature since the increasing annealing temperature leads to the additional PbI_2 formation, which is detrimental to the photovoltaic performance.[7] The electronic properties of the individual materials as well as the morphology of perovskite layer are the key factors for the device efficiency and performance. In particular, transport pathways for both photogenerated electrons and holes are strongly affected by changes in the morphology. Therefore, having a microscopic fundamental understanding of how the morphology of perovskite layer impacts on the charge extraction and the photovoltage is imperative in order to further design the device structure and improve the device performance.[8]

On the other hand, various scanning-probe microscopy (SPM) methods, such as scanning Kelvin probe microscopy (SKPM), offer the ability to correlate local optoelectronic properties with local film structure in organic electronic devices and it can study the physics of surfaces on the nanometer scale, even down to the atomic level.[9] Previously, this technique has been successfully applied for the study of topography and photoresponse in the blended bulk heterojunction organic solar cells. Several important physical processes occurring in these devices, such as phase separation,[10] networks for carrier transmission,[11] local heterogeneity,[12] and so on, have been systematically investigated. The high lateral resolution of the SPM

Dr. Z. Zhao, Prof. X. Chen, Prof. G. Cao
Beijing Institute of Nanoenergy and Nanosystems
Chinese Academy of Sciences
National Center for Nanoscience and Technology
Beijing 100083, P. R. China
E-mail: chenxiangyu@binn.cas.cn;
gzcao@u.washington.edu
Dr. Z. Zhao, Prof. H. Wu, Prof. X. Wu
Institute of Microelectronics
Tsinghua University
Beijing 100084, P.R. China
Prof. G. Cao
Department of Materials and Engineering
University of Washington
Seattle WA 98195-2120, USA

www.MaterialsViews.com

ADVANCED
FUNCTIONAL
MATERIALS
www.afm-journal.de

FULL PAPER

technique allows one to directly measure spatial variations of the electrical properties of the devices and to gain insight into the operation mechanisms which cannot be obtained from the measurement of the completed devices. The SPM application for the study of the PSCs is also a promising approach for clarifying the morphology impacts on the overall performance of the devices. Recently, Ginger group has discovered that the grain boundaries exhibited fast nonradiative decay by employing confocal fluorescence microscopy to scan the different domain of the perovskite layer, which can serve as good guidance for the further design of the PSCs.[13] Hence, the SPM technique combined with optical excitation can be a useful experimental method for elucidating a variety of structural and electronic correlations in the photovoltaic devices, such as organic polymer solar cells, PSCs, and so on.

In this paper, we applied the SPM techniques to follow the evolution of the surface potential, photogenerated voltage, and photocurrent networks of the PSCs with different film topography. First, noncontact SKPM was employed to measure the surface potential and the generated surface photovoltage with a lateral resolution better than 100 nm and the results were correlated with different topography of the PSCs. Then, the photoconductive atomic force microscopy (pcAFM) was used to map local photocurrents on the different location of perovskite layer, in order to further analyze the variation of the overall performance of the PSCs with different surface morphology. The SKPM coupled with pcAFM measurement can show us an in-depth understanding about the nanoscale photovoltaic performance as well as the effect of the morphology changing on the overall performance of PSCs.

2. Results and Discussion

Figure 1 shows the SEM images and 3D topographical images of the surface of perovskite-based films. The grain size can be tuned and well controlled by varying the concentration of $CH_3NH_3PbI_3$ solution. As observed from the SEM images, three kinds of films with different $CH_3NH_3PbI_3$ grain sizes as well as surface roughness were prepared. The grain size decreases from 500 to 400 nm and to 150 nm with the increasing concentration of the CH_3NH_3I solution from 6 to 9 to 12 mg mL^{-1}, respectively. This is well explained by the fact that high density of $CH_3NH_3PbI_3$ crystal nuclei is formed initially with high CH_3NH_3I solution concentration, which results in the growth of a large number of small $CH_3NH_3PbI_3$ crystallites or particles with narrow size distribution, whereas the small number of $CH_3NH_3PbI_3$ crystal seeds generated with low solution concentration produce large particles with wide size distribution as widely reported and well documented in the synthesis of nanoparticles.[14,15] A large number of small uniformly sized crystallites form a closed pack film while a small number of large particles with wide size distribution form a film with low coverage, agreeing very well with the results reported in the literature.[14] The 3D topographical images of these perovskite films (scale: 5×5 μm^2) have been analyzed by means of SKPM and the measurement results are shown in Figure 1c,f,i. The decreased roughness from 52 to 25 nm to 15 nm films was found to correspond well with the decreasing perovskite grain

size from 500, 400, to 150 nm. Obviously, perovskite particle size was the main factor in determining the morphology or the roughness of the perovskite film. For the sake of clarity, the perovskite-based films have been denoted as P52, P25, and P15 according to their roughness. The current–voltage (I–V) curves of the three types of solar cells were registered and their performance parameters were listed in Figure 1k. Three different I–V characterizations can be observed from Figure 1j. The J_{sc}, V_{oc}, and power conversion efficiency varied with 14.8–19.8 mA cm^{-2}, 0.94–1.0 V, and 7.4–12.3%, respectively. The P25-based cell exhibited the best performance with the highest J_{sc} (19.8 mA cm^{-2}) and fill factor (63%). However, its V_{oc} was a little lower than that (1.0 V) obtained from the P15-based cell. In our experiment, the only difference between three samples was the grain size and the coverage change of the perovskite capping layer, and we attribute the change of V_{oc} to the variation of morphology. The present research has revealed that both incomplete coverage and grain boundaries would have negative impacts on the power conversion efficiency, with increased charge recombination and increased transport resistance. Similar results have also been reported in the literature by other groups; for example, Wang's group found that the grain size could be controlled by applying DMSO solution in PbI$_2$ precursor solution and a 17.16% efficiency and stabilized power output of over 16% within 240 s could be obtained by the perovskite solar cell with an ultraflat and dense perovskite film covered onto the porous TiO$_2$ layer.[16] Furthermore, the performance of the planar heterojunction perovskite solar cell was also affected by perovskite morphology. It has been reported that a continuous uniform film could improve the V_{oc} and I_{sc} dramatically.[17] In our work, the P52-based device with the largest perovskite grain size shows the lowest V_{oc}, while the P15-based one with the smallest grain size and highest surface coverage rate shows the highest V_{oc}. We found that the V_{oc} could be increased with the decrease of the grain size. However, only a few publications analyzed and discussed such results in nanoscale resolution. By combining SKPM and pcAFM measurements, we have elucidated the details of such result. In order to get reliable and repeatable data, we also have elaborated on measurement ten sets photovoltaic performance of perovskite solar cell devices with every morphology. Herein, we added the corresponding statistical figures (Figure S1, Supporting Information). However, the question arises as to why the grain size and morphology influence power conversion efficiency when possessing the same architecture for these PSCs.

The SKPM was used to investigate the surface potential of perovskite capping layer both at dark and under illumination shown in **Figure 2**, in order to gain an in-depth understanding of the correlation between the perovskite morphology and the photovoltaic performance. **Figure 3** displays the 2D images of the topographies and potential differences measured on the perovskite-based films with different roughness at dark and under illumination. Ideally, in dark condition, no charges are expected to be generated in the film, and therefore the energy band should not bend; the surface potential should be constant across the device and equal to the work function difference between the SKPM tip and the fluorine-doped tin oxide (FTO) bottom electrode. However, the depletion zone would form between porous TiO$_2$ layer and perovskite capping layer, which
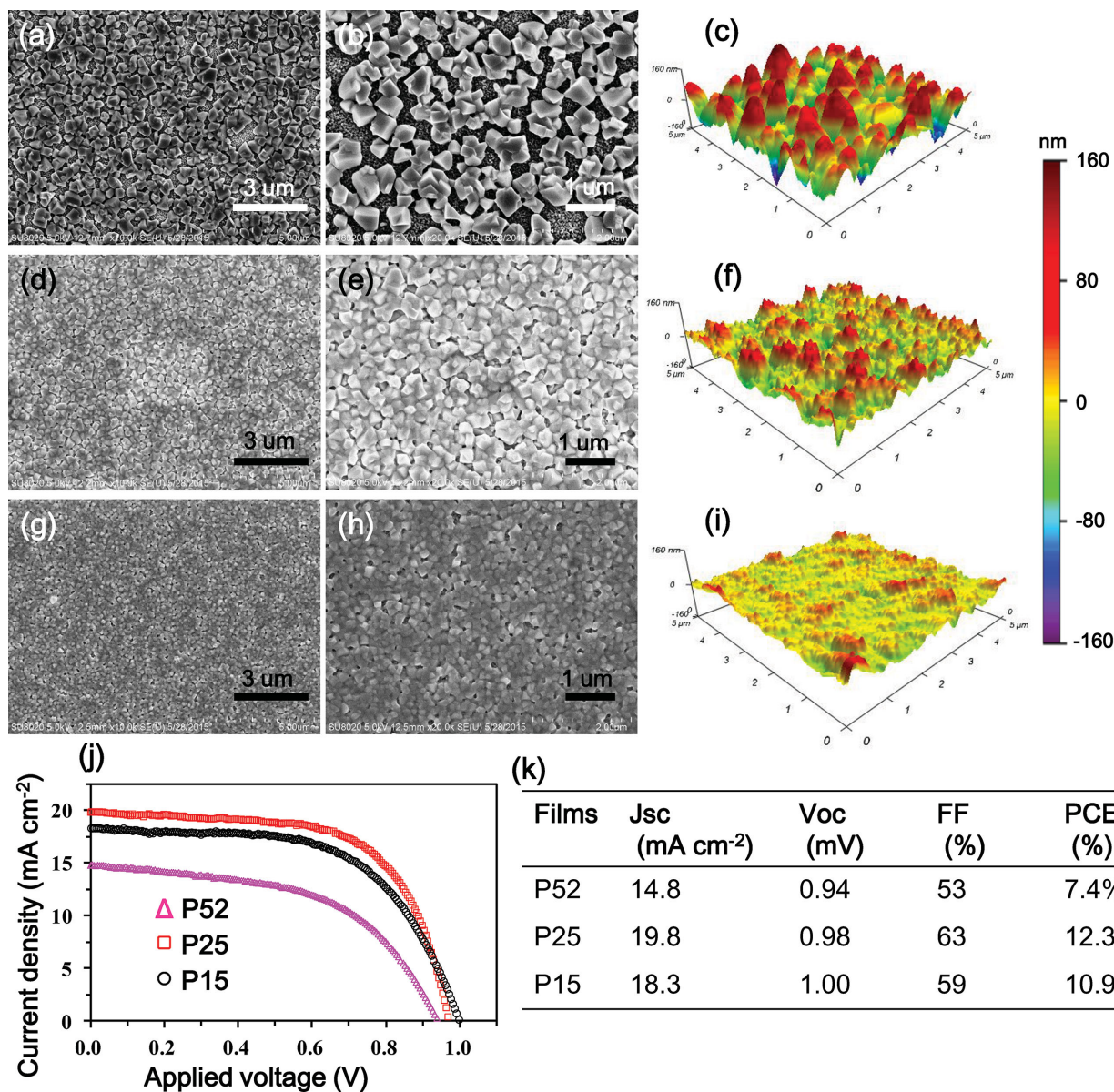
Figure 1. Three of the perovskite-based films with different roughness and coverage rate have been studied in this experiment. a,d,g) The low and b,e,h) large magnified SEM images of the film surfaces and c,f,i) their corresponding 3D AFM images. The roughness was 52, 25, and 15 nm for (a–c), (d–f), and (g–h) films, respectively. For clarification, they are noted as P52, P25, and P15. j) I–V curves measured for the perovskite solar cells employing these P52, P25, and P15 films from 0 to 1 V bias voltage with 200 ms speed rate under AM 1.5 G one sun (100 mW cm^{-2}). k)Photovoltaic parameters obtained from I-V curves.

would result in the variation of the built-in potential as well as the surface potential inside the sample. As reported by the previous study,[18] the depletion zone in the perovskite side extends ≈300 nm, which is larger than the thickness of the capping layer in our PSCs. We also measured the potential changing along the thickness direction by using a similar method, as can be seen in Figure S4 (Supporting Information). Hence, with the increase of the thickness of the capping layer, the built-in potential inside the PSCs would increase due to the extension of the depletion region. Accordingly, by comparing the topography and the differential potential images (Figure 3), the fluctuation of the surface potential exhibited a very similar feature

as the topography of the perovskite-based films; specifically, large potential differences appeared in the high position of the surface film, whereas low ones arise from the low position.

Furthermore, the zoom-in SKPM results are shown in **Figure 4** The potential differences of perovskite films were found to be strongly affected by their roughness, seen by comparing the curves of potential difference (Figure 4B) and their corresponding morphologies (Figure 4C). Additionally, the potential differences taken under illumination were larger than those acquired at dark in all films with different roughness. It confirmed the presence of photovoltaic effect for perovskite-based film, and the average potential differences (ΔV)
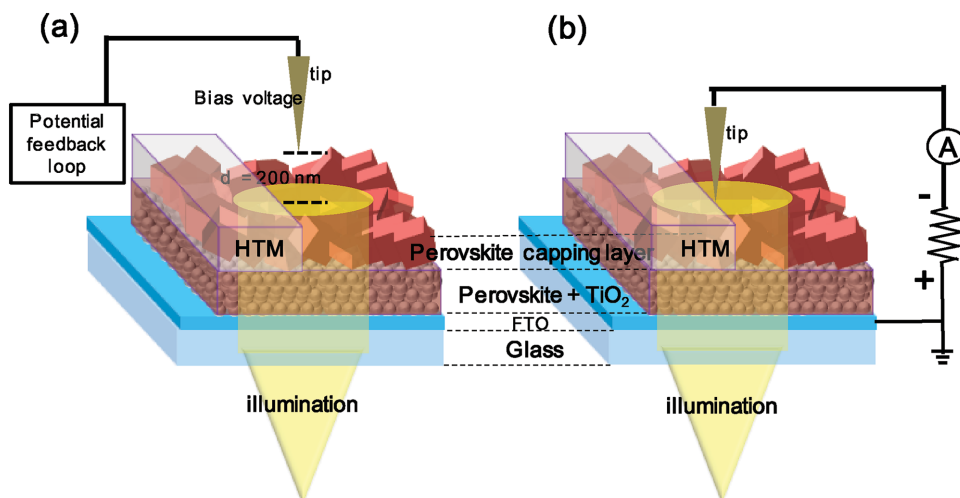
Materials Views
www.MaterialsViews.com

ADVANCED
FUNCTIONAL
MATERIALS
www.afm-journal.de

FULL PAPER

Figure 2. a) Experimental schematic of the Kelvin probe force microscopy (SKPM) equipped with a switchable illumination to test potential difference between tip and samples, as well as the topography images. b) Experimental schematic of the photoconductive atom force microscopy (pcAFM). The applied voltages between the FTO substrate and the conductive probe tips were 0 V. The selected SKPM mode is collecting the Kelvin probe and topographical signals simultaneously at two different tip oscillation frequencies. The distance d and bias voltage employed on tip used to measure potential signals are 200 nm and 700 mV, respectively. A switchable light (1.5 G AM sun light, 104 mW cm^{-2}) was equipped under the glass substrate to meet the illuminated condition.)

between the dark and illuminated condition are related to the photoresponse of the perovskite film. As shown in Figure 4B, a surface potential profile reveals a clear increase of potential variation (positive shift) with incident light. We attribute this positive value to a net transfer of negative charges to the back contact (connected to the ground in our setup) resulting in a global positive shift. A similar effect can be found in ref. [19] Based on the potential differences (Figure 4B), the average differences between the potential difference obtained under illumination and the one acquired at dark (ΔV) for three different samples were calculated, which are 125, 67, and 29 mV for P52, P25, and P15 samples, respectively. The detailed value of ΔV cannot be directly converted to the value of the V_{oc}, while it can be considered as the exhibition of the strength of the photovoltaic effect.[9] As reported by previous studies, [20,21] SKPM measurements of the surface potential of active layer with respect to different light intensity follow a similar changing tendency with the actual open-circuit voltage of devices made from the same films. Hence, it is interesting to find out that the changing of the surface potential is not in good agreement with the obtained V_{oc} form of the complete device. As shown in Figure 4, the P52 film with the largest grain size showed the mose significant ΔV in comparison to the smallest V_{oc} obtained by photovoltaic performance measurements (Figure 1). The large grain with large thickness means more material, which would absorb more illumination energy or photons and generate more photocarriers. Therefore, in our SKPM measurements (see Figure 3b), the P52 sample with larger grain size showed most significant change of the surface potential with respect to the incident light under illumination, indicating that P52 sample has stronger photovoltaic response and the potential to provide higher PCE. However, the SKPM measurements on the surface of perovskite capping layer were not in accordance with the $I–V$ measurements of the completed solar cell devices, implying the interfacial phenomenon happened on the

interface between perovskite film and the transport material layer (HTL) accounting for the suppression of the performance of the PSCs. Actually, the disagreement between SKPM and $I–V$ results is just one of the motivation for our next investigation. We hope to clarify the underlying mechanism by using the pcAFM technology. Even though the photoinduced potential variation observed from SKPM could not be used to directly illustrate the strength of the V_{oc} in the complete devices, it provides useful indication of the potential of P52 perovskite film for generating a high V_{oc}. It might be possible to enhance the V_{oc} of the device by analyzing and modifying the interfacial properties of the P52 perovskite film.

We deposited the HTL onto the surface of the perovskite capping layer and made a further investigation by employing the SKPM measurements on the surface of the HTL based on three different films (**Figure 5**). The surface potential differences of the HTL were unified and showed little variation on the surfaces with obvious morphological change. In other words, the surface potential difference of the HTL was not influenced by the surface morphology. It can be attributed to the screen effect of the free carriers transported into the HTL.[20,22] In other words, The HTL is the film for holes transporting and the carrier extraction. There will be almost no direct photocarrier generation inside the HTL. Hence, even if there is no light that can pass through the absorbing layer, the photogenerated holes will still transport to the film of HTL. That is the reason that nanoscale mapping techniques, such as pcAFM and SKPM, are usually applied on the dielectric film rather than the charge transporting layer. It is important to note that the observed potential changing (ΔV) between dark and illuminated condition on the surface of HTL is totally different from those obtained from the perovskite capping layer shown in Figure 3. The values of the ΔV change in the order of P15 > P25 > P52. This was in good agreement with the changing tendency of the V_{oc} which suggests that the ΔV observed by SKPM is illustrative

**ADVANCED
FUNCTIONAL
MATERIALS**

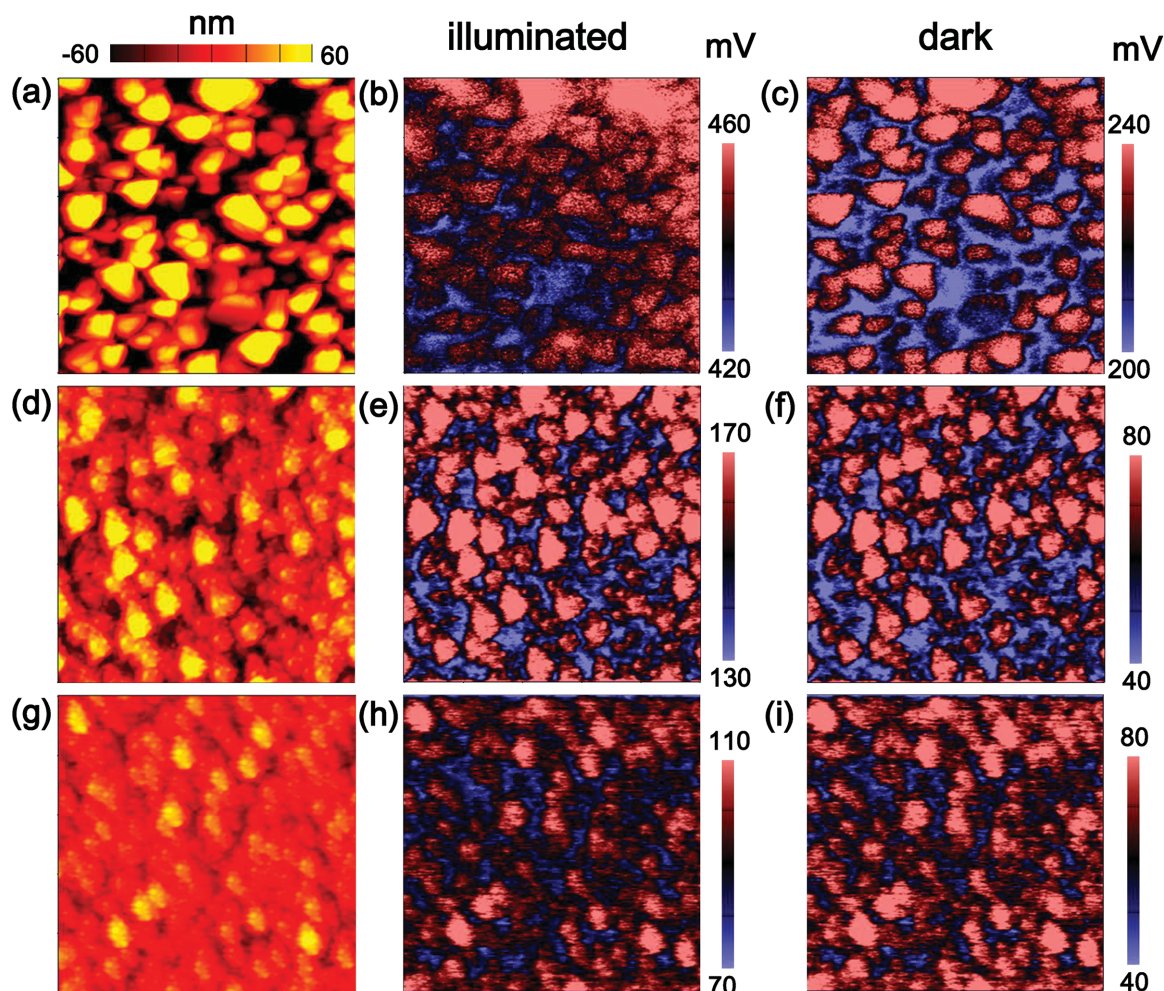www.afm-journal.de

*Materials
Views*

www.MaterialsViews.com

Figure 3. a,d,g) Topographical and b,c,e,f,h,i) potential difference 2D images of the (a–c) P52, (d–f) P25, and (g–i) P15 films (scale: 5 × 5 µm²). The potential differences were recorded (b,e,h) under illumination and (c, f,i) in dark.

of the strength of the photovoltaic effect. Meanwhile, the different data of the ΔV shown in Figure 4 and Figure 5 also further confirmed that the interfacial interaction happened on the interface between perovskite layer and HTL is likely the reason that the V_{oc} of P52 sample was suppressed.

In order to further clarify the effect of the nanoscale morphology on the performance of the PSCs, the pcAFM was performed on the surface of perovskite capping layer, which used the same experimental set up as schematically illustrated in Figure 1 Samples were imaged with an SPM mode and the current was recorded by its internal preamplifier (Asylum Research, ORCA head model) with illumination. **Figure 6** shows a pcAFM image collected from the perovskite capping layer with the morphology of P25, where both a typical SKPM scan and its associated current probing at different position on the film were obtained by using the photoexcited pcAFM technique.[11,12] The height and short-circuited photocurrent mapping pictures with illumination at 104 mW m⁻² intensity are shown in Figure 5a,b. The photocurrent is high inside the grain region of perovskite film (high-topography regions) but low in the grain boundary regions (low topography regions). The current-voltage data were also recorded in the dark or under

illumination. Figure 5b shows a photoexcited pcAFM image with high spatial resolution. In order to further study the generation of the photo-current in nanoscale resolution, we selected three representative positions on the surface of the perovskite capping layer. Herein, we selected these locations on the surface of P25 sample. The P25 sample has the highest power conversion efficiency and the detailed analysis of this sample may help us to further enhance the maximum PCE of our fabricated sample. Three selected positions are marked in Figure 5a,b and they are the center positions of a grain (blue), the grain boundary (red), and the defect part of the perovskite capping layer (green). These positions are most representative of all the three samples and the related pcAFM analysis can also be applied to three different samples. It is noted that these probing positions are all selected on the P25 film. The results of the probed nanoscale I–V performance of different positions are presented in Figure 5c,d. The light absorption and the charges generation happened most significantly inside the perovskite crystal grains. Accordingly, the region inside the grain exhibited significant photovoltaic performance under the illumination shown in Figure 5c, while the grain boundary and the defect position showed much less, nearly no photoresponse. Since
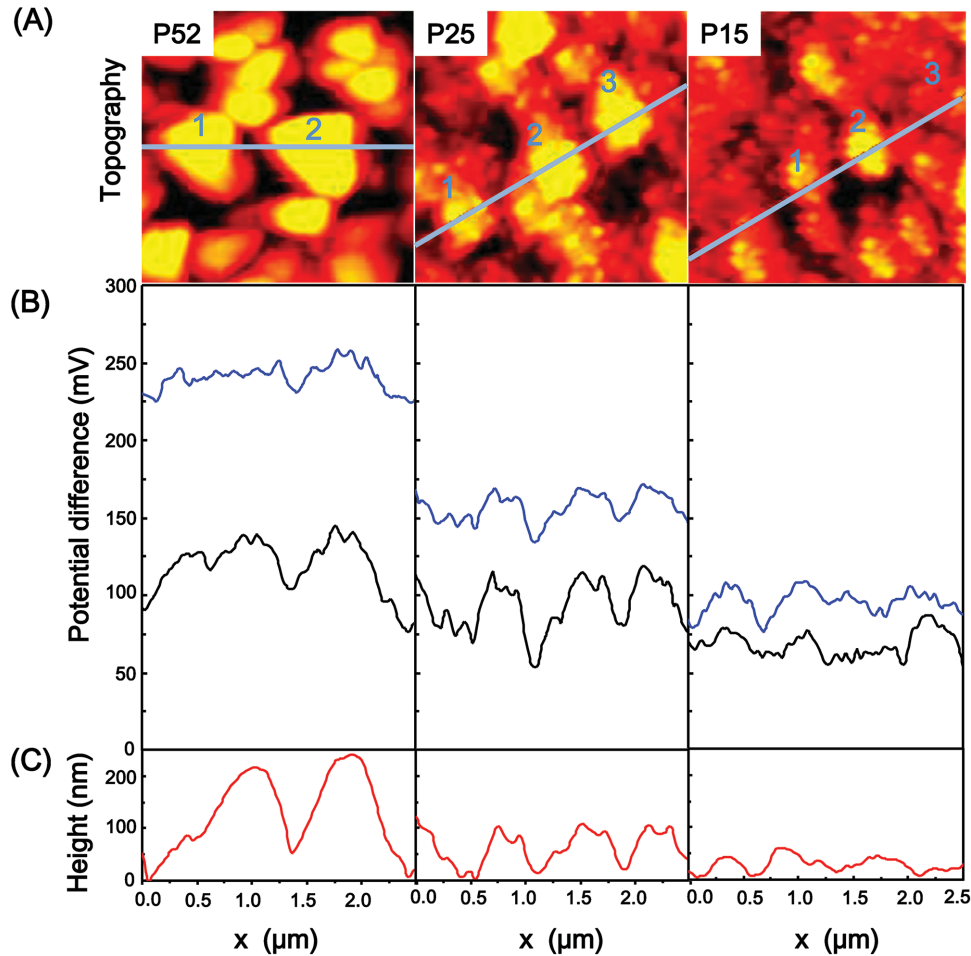
Materials
Views
www.MaterialsViews.com

ADVANCED
FUNCTIONAL
MATERIALS
www.afm-journal.de

FULL PAPER

Figure 4. A) Topographical 2D images of P52, P25, and P15 films and B) their corresponding potential difference curves in dark (black line) and under illumination (blue line), as well as C) their height profiles along with the selected line labeled in topography images.

the perovskite capping layer has good buffering performance, the lowest dark current could be obtained inside the grains. However, the obtained variation regulation of nanoscale photoresponse could be applied to other films with different roughness due to a similar material and architecture in all these films (P51, P25, and P15). We also did similar pcAFM measurements on the P52 and P15 samples (similar positions), shown in Figures S5 and S6 (Supporting Information), where the same changing tendency of photocurrent was observed and only the detailed amplitude of the currents is different: that is, the photocurrent intensities were higher on the center of the grain than on the defect position, whereas the larger grain size leads to the higher photocurrent on the center. Meanwhile, the dark current intensities increased dramatically in the defect position, suggesting a high conductive character for defect position.

To study the photocurrent generation, the effective photocurrents at three positions were measured using pcAFM system. The devices were biased in a sweep voltage ranging from +1 to −2 V. Figure 5e shows the effective photocurrent (I_{ph}) as a function of the effective bias ($V_{eff} = V_0 − V$), where V is the externally applied bias and V_0 is the bias where the illuminated current is equal to dark current crossed ($I_{light} = I_{dark}$).[23] I_{ph} was obtained by correcting the current under illumination for the dark current,

i.e., $I_{ph} = I_{light} − I_{dark}$. In the low effective field region ($V_{eff} <$ 0.2 V), the I_{ph} increased linearly with the effective bias voltage, which is similar to the researches with completed solar devices reported earlier in the literature.[22] At large reverse bias (V_{eff} > 1.5 V), I_{ph} saturated for all the positions, while the position inside the grain possessed the highest saturated photocurrent (I_{sat}) and the I_{sat} in the defect region was close to zero. The maximum generation rates (G_{max}) of electron–hole pairs are given as $J_{sat} = e\ G_{max}L$, where J_{sat} and L are the saturated photocurrent density and the thickness of perovskite layer, respectively.[22] The G_{max} in the central part of the grain was about 1.4×10^{31} m^{-3} s^{-1}, whereas the weakest one generated in the defect region, suggesting that the thickness of the capping layer in this region is close to zero. These results demonstrated that the perovskite capping layer served as the absorption layer for the photoexcitation, supporting the concept of p-i-n structure of the PSCs described by Meng's group.[24]

To better compare the photocurrent at different locations and understand the relationship between photocurrent and morphology, we have plotted the normalized photocurrent (J_{ph}/J_{sat}) for three different positions in Figure 5f. Based on Onsager's theory[25] of ion-pair dissociation in weak electrolytes, a certain fraction of photogenerated exciton will dissociate
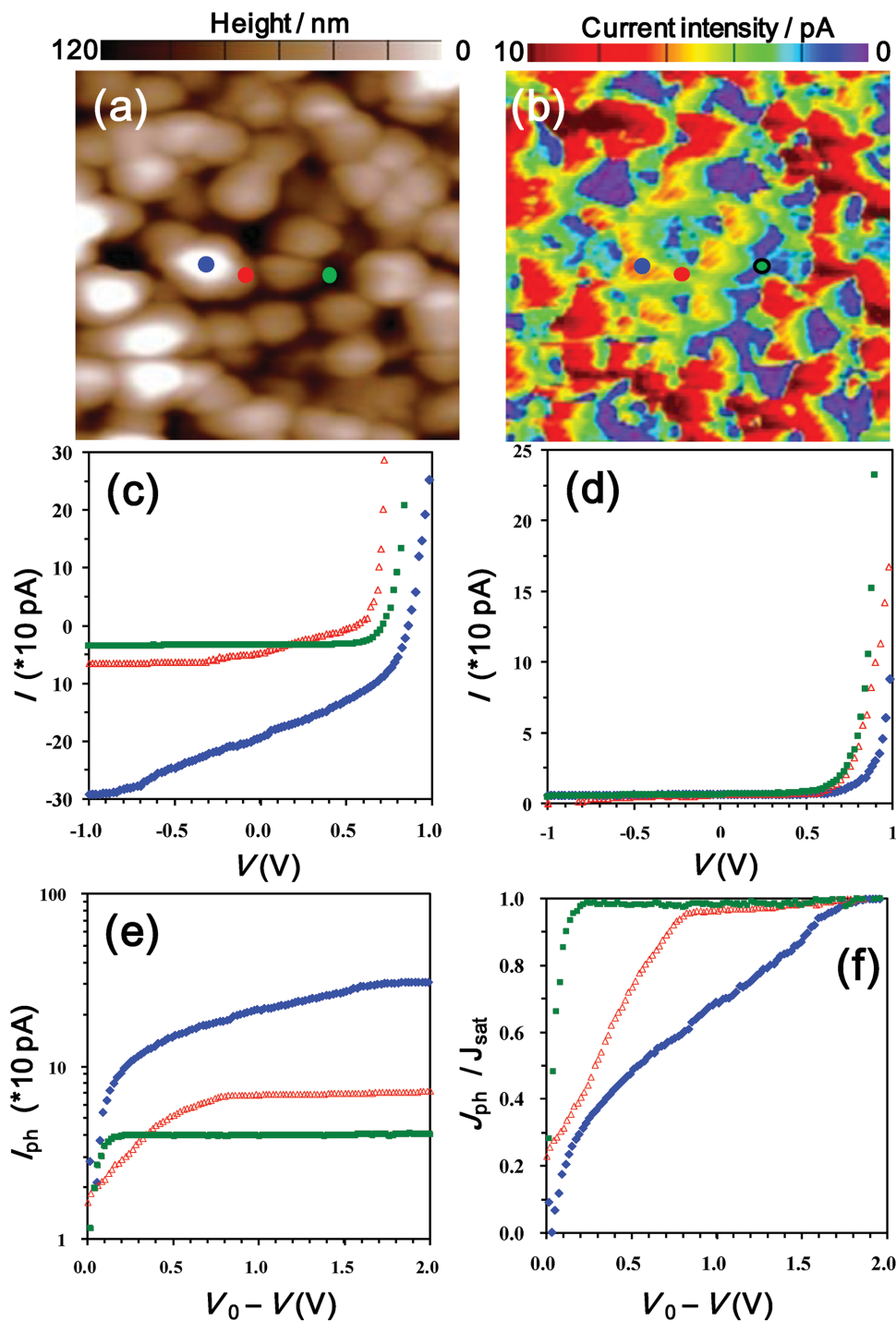
Figure 5. a) Topographical and b) current intensity mapping images of the perovskite capping layer of the P25 film without HTL deposition. Three dots including top interface, and defect of perovskite crystalline were selected and labeled as blue, red, and green, respectively. Current intensities obtained by pcAFM measurement depending on bias voltage from −1 to 1 V under c) illumination and d) dark condition. e) Plots of photocurrent intensity (J_{ph}) and f) their corresponding plots of J_{ph}/J_{sat} with respect to effective bias (V_0-V).

into free carriers with a dissociation probability P (E,T). The exciton dissociation is facilitated by the interface or the build-in electric field and the saturation of the photocurrent will be delayed in the case of imperfect P (E,T). However, for the perovskite's case, the previous exciton model may not be effective

since the excitonic phenomenon of perovskite is still an open question.[26,27] The exciton binding energies for $CH_3NH_3PbI_3$ have been reported in the range of 55 ± 20 meV at room temperature,[27] which may be smaller than ambient thermal energy (kT, k: Boltzmann constant) and thus the photoexcited

www.MaterialsViews.com

www.afm-journal.de

ADVANCED
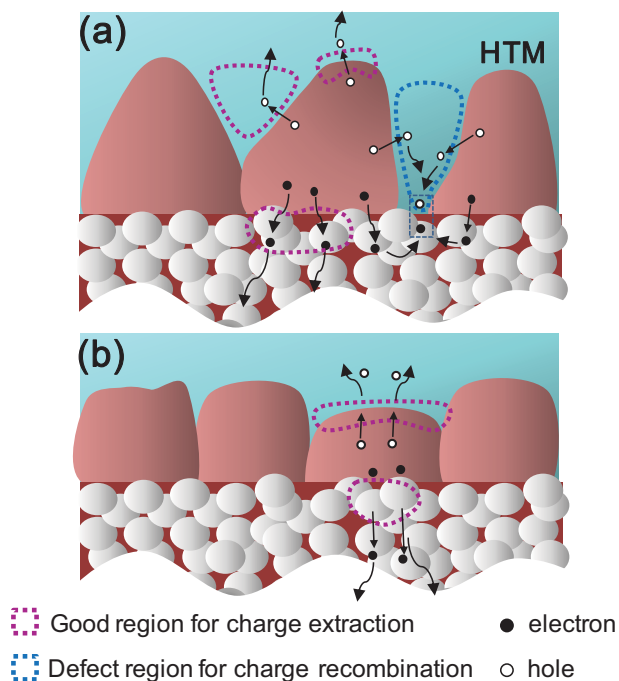FUNCTIONAL
MATERIALS

FULL PAPER

Figure 6. Schematic of the charge extraction and recombination inside the PCSs with a) rough perovskite capping layer and b) smooth one. The electrons (•) and holes (○) excited inside the perovskite particles will transport to the n-type TiO$_2$ layer and HTL, respectively. However, carries in the good regions noted in pink circles have good migration ability, whereas in the defect regions noted in blue circles exhibit stronger recombination.

electron–hole pairs have the high possibility to be dissociated very fast into free charges. The previous study has also demonstrated that free charges are formed within 1 ps of photoexcitation in the mixed halide perovskite CH$_3$NH$_3$PbI$_{3-x}$Cl$_x$ at room temperature.[28] Hence, even though the existence of the excitonic phenomenon of perovskite is still debatable, it has been well proved that the dissociation probability of electron–hole pairs inside the pristine perovskite is close to 100% due to the small exciton binding energy.[28] Accordingly, the Onsager theory may not be valid in the perovskite system. As shown in Figure 5f, the region inside the grain showed the highest J_{sat}, while the saturation process of the photocurrent was delayed significantly. As marked by the dashed line in Figure 5f, only 60% of the photogenerated free charges can be extracted to the external circuit at the short-circuit condition. This suggests that about 40% of the generated e–h pairs were lost in the active layer before being extracted. Since the free charges instead of exciton are predominantly generated in the photoexcited PSCs, the electron–hole recombination caused by the multiple collisions of the free carriers[28] can be the reason for this insufficient charge extraction. It also suggests that the extraction of the photogenerated carriers in neat perovskite layer still requires help from the heterojunction interfaces and, thus, the thick capping layer is deemed to increase the decay of the photogenerated carriers. As also shown in Figure 5e,f, the photocurrent in the defect region and the grain boundary saturated very fast, while the J_{sat} at these two regions are rather small (the G_{max} are small in these region). At the short-circuit

condition ($V_{eff} = V_0$), over 95% of the photogenerated carriers can be extracted to the external circuit in these two regions, which suggests that the charge extraction was facilitated due to the decrease of the carrier recombination possibility (the small G_{max} will decrease the recombination possibility). Meanwhile, it is interesting to note that this rapid saturation of the photocurrent was not a typical exciton dominated photovoltaic process, since the reverse bias can usually facilitate the exciton dissociation and further increase the photocurrent.[23] More importantly, as show in Figure 5c,d, the defect region of capping layer showed very insignificant photoresponse, while the conductivity of these region is quite high in the dark condition. Therefore, the defect region of the perovskite capping covered by the HTL may strongly suppress the photovoltaic process. In our performance measurements, the efficiency of the P52-based device with larger grain size decreased dramatically in comparison with those of the P25 and P15-based devices. The larger grain size usually yields a better performance.[29] It is also proved by our SKPM measurement (Figure 4b), where P52 sample with larger grain size showed most significant changing of the surface potential with respect to the incident light, indicating that P52 sample has stronger photovoltaic response and the potential to provide higher PCE. However, the perovskite crystal particle was not the only factor to affect the performance. As can be seen in Figure 1, more defect regions were found in the capping layer of the P52-based film than those in the P25 and P15 films. As analyzed by the pcAFM measurement results, these defect regions can work as the recombination center to consume the photoenergy, which can explain the suppression of the performance of the P52-based complete device. Therefore, an ideal structure of the PSC should have big grain size and without defect region,[27] which can maintain significant photovoltaic reaction and less recombination of the photocarriers.

Figure 5c reveals that the defect region of the capping layer shows little photovoltaic response under the illumination, while this region exhibits high conductivity in dark condition (see Figure 5d), which can be a negative effect for the PSCs performance. In this case, the defect region would work as a recombination center for the photogenerated charges in the surrounding region. Knowing that photogenerated holes can move freely in the HTL and the defect region of the capping layer also has high conductivity under the illumination, the direct contact between them will establish the current paths for the recombination of the photogenerated charges. These recombination processes become more serious under open-circuit condition and they can suppress the overall V_{oc} of the complete device. The sketch of these recombination processes is described in the defect region shown in **Figure** 6a, where the thickness of the capping layer in the defect region is close to zero, as suggested by the pcAFM measurement in Figure 5. On the other hand, the perovskite capping layer with better coverage (Figure 6b) would prevent the recombination of the photogenerated charges due to its buffering function, and the holes and the electrons will be transported to the top hole transport layer (holes) and bottom electron transport layer (electrons) of the device, respectively, to establish an open-circuit voltage.[30] The favorable charge extraction processes are also described in Figure 6b. The capping layer does serve multifunctions in the solar cells. In a word, the main function of the perovskite capping layer is for

FULL PAPER

light harvesting. In our research, we also find that there are a lot of defects on the capping layer due to the insufficient coverage rate. These defect regions can serve as the recombination centers to consume the photogenerated charges. On the other hand, for the capping layer without defects, the charge recombination is prevented largely due to the buffering effect of the capping layer. In this case, the capping layer serves as a barrier to avoid recombining between electrode and hole captured by ETL and HTL. Therefore, for the three different morphologies, the P15 film with the smoothest capping layer showed the highest V_{oc}, while the P52 one with the largest grain size and the roughest surface possessed the smallest V_{oc}, which is due to the charge recombination at the defect region.

As can be seen in Figure 1j,k, the variation of J_{sc} in three different films was more complicated in comparison with that of V_{oc}. It is easy to understand that the P52-based film with the roughest surface has the lowest J_{sc}. However, the J_{sc} (19.8 mA cm^{-2}) of the P25-based PSC was slightly larger than

that (18.3 mA cm^{-2}) of the P15-based one, even though the P15 film has the smoothest perovskite capping layer. The light absorption was determined by the thickness of the capping layer (**Figure 7**e,f). The slight suppression of J_{sc} exhibited in P15 film could be attributed to the less light absorption caused by the decrease in the thickness of the perovskite capping layer. If we consider the net absorption across the lateral surface, the P15 sample should have a better absorption rate, due to the more compact surface structure. However, the smaller grain size of the P15 sample also significantly decreased the absorption in the thickness direction. Hence, the compact surface could not solely grantee better utilization of the photoenergy. Meanwhile, it is true that the absorption process concerned with several effects and further in-depth analysis is still necessary for the study. Another possible reason for the suppression of the J_{sc} may relate to the increase of the grain boundary region. The smallest grain size in P15 film would generate more grain boundary regions in the perovskite capping layer.
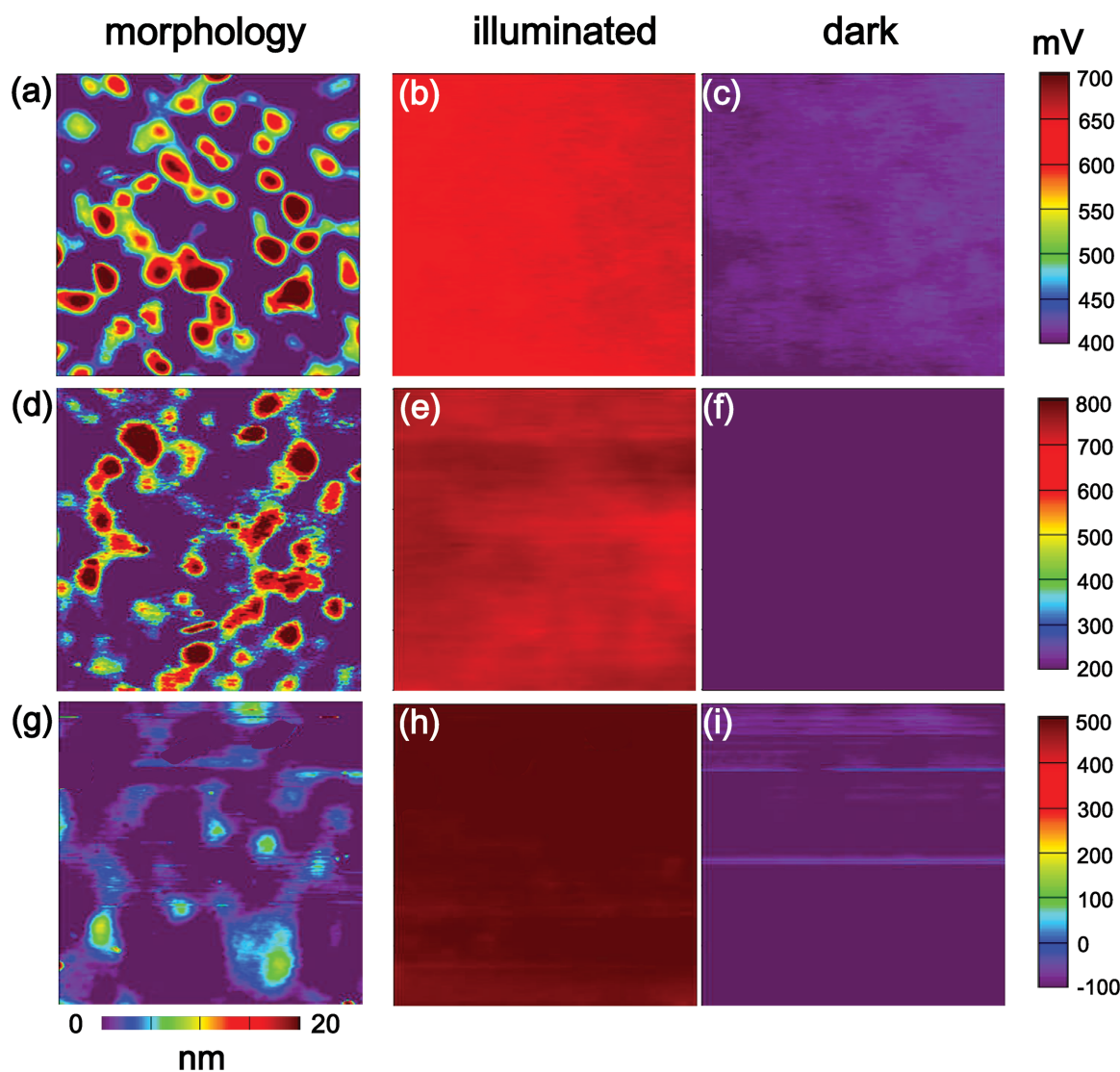

Figure 7. a,d,g) Topographical and b,c,e,f,h,i) potential different 2D images of the (a–c) P52, (d–f) P25, and (g–i) P15 films (scale area: 5 × 5 μm^2) with HTL. The potential differences were recorded (b,e,h) under illumination and (c,f,i) in dark.

www.MaterialsViews.com

ADVANCED
FUNCTIONAL
MATERIALS
www.afm-journal.de

FULL PAPER

As demonstrated in Figure 5e, the generation of photocarriers in the grain boundary region was not effective and, thus, the increased grain boundary region results in the suppression of the overall charge generation, which leads to the suppression of the I_{sc}. Therefore, the smaller grain size could maintain a high V_{oc} for PSCs by eliminating the defeat region in the capping layer; on the other hand, it would suppress the I_{sc} generation by increasing the boundary region in the capping layer. A well-designed nanoscale morphology of the perovskite capping layer is one of the key factors for achieving high power conversion efficiency in PCSs.

3. Conclusions

The SKPM technique coupled with pcAFM has been demonstrated as a powerful tool for mapping and analyzing the photovoltage and photocurrents with nanoscale resolution. Three kinds of perovskite $CH_3NH_3PbI_3$ capping films with different morphologies and crystallite sizes as well as the corresponding complete PSC devices based on those three films were prepared. On the basis of SKPM and pcAFM measurements with nanoscale resolution, we give specific and in-depth analysis of several interfacial phenomena of PSCs and their effect on the performance of the complete devices, including the variation of surface potential correlated with morphology, the photovoltaic reaction on different interface, the localized photocurrent generation, and so on. It has been found that the defect regions on the capping layer with good conductivity showing little photovoltaic response, which can establish small current paths for the photo-charge recombination. Accordingly, even though the P52 film with the largest grain size shows the most significant photovoltaic response in the SKPM measurement, the V_{oc} of P52-based PSCs was suppressed due to the existence of defect regions. Meanwhile, the insufficient charge generation in the grain boundary region was also observed by the pcAFM measurements. Hence, P15 film with the smallest grain size can eliminate the defect region, while it can also reduce the I_{sc} due to the increase of the grain boundary region. For perspective, the favorable nanoscale morphology for the perovskite layer film requires some elaborate optimization processes in order to achieve high performance of the PSCs and SPM techniques, such as SKPM and pcAFM, can serve as good guidance for the optimization of the interfacial nanostructure of the perovskite films.

4. Experimental Section

The perovskite-based films with the configuration FTO/compact TiO_2/mesoporous TiO_2+$CH_3NH_3PbI_3$/$CH_3NH_3PbI_3$ and FTO/compact TiO_2/mesoporous TiO_2+$CH_3NH_3PbI_3$/$CH_3NH_3PbI_3$/hole HTL were prepared. Typically, FTO glasses were cleaned with detergent, followed by sonicated subsequently in a bath with acetone and ethanol. Then, plasma O_2 cleaner was used to remove organic impurities for 20 min under 200 Hz. A compact TiO_2 blocking layer was deposited on the cleaned FTO substrate by atomic layer deposition (ALD, Picosun SUNALE R-100). Herein, $TiCl_4$ and N_2 were used as Ti source and purging gas, respectively. Compact TiO_2 with 25 nm thickness was grown on FTO substrate with 500 ALD cycles at 200 °C deposition temperatures.

TiO_2 paste (Dyesol-18NRT) was diluted with ethanol in 2:7 ratios in weight and spin-coated onto the compact TiO_2 layer on FTO substrate in 5500 rpm and sintered at 500 °C for 30 min to form mesoporous TiO_2 layer with 300 nm thickness. PbI_2 was infiltrated into mesoporous TiO_2 layer by spin-coating with PbI_2 in N,N-dimethylformamide (DMF) solution (462 mg ml^{-1}) and kept at 70 °C. After drying, the films were dipped in a CH_3NH_3I solution in 2-propanol for 30 s and sintered at 70 °C for 30 min. It is known that the grain size of $CH_3NH_3PbI_3$ in capping layer can be controlled by changing the concentration of CH_3NH_3I solution.[14] In this experiment, the 6, 9, and 12 mg mL^{-1} were selected to fabricate $CH_3NH_3PbI_3$-based films with varying roughness. The HTL was deposited by spin-coating at 3000 rpm for 30 s with Spiro-OMeTAD solution. This solution was prepared by dissolving 73.5 mg Spiro-OMeTAD powder into 1 mL chlorobenzene. Then, 28.8 µL tBP and 17.5 µL Li-TFSI in acetonitrile (520 mg L^{-1}) were added into it.

Characterization: The light source was calibrated to AM 1.5 sun with 100 mW cm^{-2} intensity. In order to measure the *I–V* characteristic curves, 80 nm thickness of gold was deposited onto the surface of the above films by a thermal evaporation with a defined device active area (3.5 cm^2).

Herein, the SKPM measurements and the pcAFM were used to study the perovskite crystal $CH_3NH_3PbI_3$ capping layers in nanometer resolution by collecting the current intensities and the potential differences at dark or under illumination. The experimental schematic of SKPM and pcAFM experiments is shown in Figure 2. PtIr$_5$ probe coated on Si cantilevers (Nanoworld, EFM, spring constant of 2.8 N m^{-1}) was used in our experiments. SKPM technique can detect and analyze the potential difference between the probe tip and the sample. A Nap mode method, including two passes—the first pass is used to determine the topography of surface and the second one which is raised above the surface testing the surface potential—was used as SKPM method. The raised distance was 200 nm in the second pass and the bias voltage applied to the tip was 700 mV. The pcAFM method can be considered as the measurement of the current passing through the tip and the sample with bias voltage applying between tip and FTO substrate. The scanning rate of the pc-AFM measurement was 0.05 V s^{-1}, which could help to rule out the influence from hysteresis effect.[31] As illustrated in Figure 2, a switchable illumination using the inverted optical microscope was focused onto the FTO glass substrate. The cross sectional view of these three devices (to analyze the thickness of perovskite film) and the light absorbed capability of these perovskite-based films by UV–vis spectrometer were also measured, as can be seen in Figures S2 and S3 (Supporting Information). The approximate thickness values were obtained by measuring layer thickness from the cross-section pictures. Therefore, the error margin was reduced by taking average value after measuring many positions.

Supporting Information

Supporting Information is available from the Wiley Online Library or from the author.

ADVANCED
FUNCTIONAL
MATERIALS
www.afm-journal.de

Materials
Views
www.MaterialsViews.com

FULL PAPER

[1] a) J. Burschka, N. Pellet, S.-J. Moon, R. Humphry-Baker, P. Gao, M. K. Nazeeruddin, M. Graetzel, *Nature* **2013**, *499*, 316; b) A. Kojima, K. Teshima, Y. Shirai, T. Miyasaka, *J. Am. Chem. Soc.* **2009**, *131*, 6050; c) M. M. Lee, J. Teuscher, T. Miyasaka, T. N. Murakami, H. J. Snaith, *Science* **2012**, *338*, 643; d) J. T.-W. Wang, J. M. Ball, E. M. Barea, A. Abate, J. A. Alexander-Webber, J. Huang, M. Saliba, I. Mora-Sero, J. Bisquert, H. J. Snaith, R. J. Nicholas, *Nano Lett.* **2014**, *14*, 724; e) J. Wei, Q. Zhao, H. Li, C. Shi, J. Tian, G. Cao, D. Yu, *Sci. China* **2014**, *44*, 801.

[2] H.-S. Kim, C.-R. Lee, J.-H. Im, K.-B. Lee, T. Moehl, A. Marchioro, S.-J. Moon, R. Humphry-Baker, J.-H. Yum, J. E. Moser, M. Graetzel, N.-G. Park, *Sci. Rep.* **2012**, *2*, 591.

[3] M. Liu, M. B. Johnston, H. J. Snaith, *Nature* **2013**, *501*, 395.

[4] O. Malinkiewicz, A. Yella, Y. H. Lee, G. Minguez Espallargas, M. Graetzel, M. K. Nazeeruddin, H. J. Bolink, *Nat. Photonics* **2014**, *8*, 128.

[5] a) N. J. Jeon, J. H. Noh, Y. C. Kim, W. S. Yang, S. Ryu, S. Il Seol, *Nat. Mater.* **2014**, *13*, 897; b) P. Docampo, F. C. Hanusch, S. D. Stranks, M. Doeblinger, J. M. Feckl, M. Ehrensperger, N. K. Minar, M. B. Johnston, H. J. Snaith, T. Bein, *Adv. Energy Mater.* **2014**, *4*.

[6] a) G. E. Eperon, S. D. Stranks, C. Menelaou, M. B. Johnston, L. M. Herz, H. J. Snaith, *Energy Environ. Sci.* **2014**, *7*, 982; b) J. H. Noh, S. H. Im, J. H. Heo, T. N. Mandal, S. I. Seok, *Nano Lett.* **2013**, *13*, 1764.

[7] A. Dualeh, N. Tetreault, T. Moehl, P. Gao, M. K. Nazeeruddin, M. Graetzel, *Adv. Funct. Mater.* **2014**, *24*, 3250.

[8] a) R. S. Sanchez, V. Gonzalez-Pedro, J.-W. Lee, N.-G. Park, Y. S. Kang, I. Mora-Sero, J. Bisquert, *J. Phys. Chem. Lett.* **2014**, *5*, 2357; b) H.-S. Kim, I. Mora-Sero, V. Gonzalez-Pedro, F. Fabregat-Santiago, E. J. Juarez-Perez, N.-G. Park, J. Bisquert, *Nat. Commun.* **2013**, *4*.

[9] L. S. C. Pingree, O. G. Reid, D. S. Ginger, *Adv. Mater.* **2009**, *21*, 19.

[10] C. R. McNeill, H. Frohne, J. L. Holdsworth, J. E. Furst, B. V. King, P. C. Dastoor, *Nano Lett.* **2004**, *4*, 219.

[11] L. S. C. Pingree, O. G. Reid, D. S. Ginger, *Nano Lett.* **2009**, *9*, 2946.

[12] D. C. Coffey, O. G. Reid, D. B. Rodovsky, G. P. Bartholomew, D. S. Ginger, *Nano Lett.* **2007**, *7*, 738.

[13] D. W. deQuilettes, S. M. Vorpahl, S. D. Stranks, H. Nagaoka, G. E. Eperon, M. E. Ziffer, H. J. Snaith, D. S. Ginger, *Science* **2015**, *348*, 683.

[14] G. Grancini, S. Marras, M. Prato, C. Giannini, C. Quarti, F. De Angelis, M. De Bastiani, G. E. Eperon, H. J. Snaith, L. Manna, A. Petrozza, *J. Phys. Chem. Lett.* **2014**, *5*, 3836.

[15] G. Cao, Y. Wang, **2012**, 41.

[16] W. Li, J. Fan, J. Li, Y. Mai, L. Wang, *J. Am. Chem. Soc.* **2015**, *137*, 10399.

[17] C.-Y. Chang, C.-Y. Chu, Y.-C. Huang, C.-W. Huang, S.-Y. Chang, C.-A. Chen, C.-Y. Chao, W.-F. Su, *ACS Appl. Mater. Interfaces* **2015**, *7*, 4955.

[18] A. Guerrero, E. J. Juarez-Perez, J. Bisquert, I. Mora-Sero, G. Garcia-Belmonte, *Appl. Phys. Lett.* **2014**, 105.

[19] a) E. J. Spadafora, R. Demadrille, B. Ratier, B. Grevin, *Nano Lett.* **2010**, *10*, 3337; b) K. P. Puntambekar, P. V. Pesavento, C. D. Frisbie, *Appl. Phys. Lett.* **2003**, *83*, 5539.

[20] M. Chiesa, L. Burgi, J. S. Kim, R. Shikler, R. H. Friend, H. Sirringhaus, *Nano Lett.* **2005**, *5*, 559.

[21] G. Shao, M. S. Glaz, F. Ma, H. Ju, D. S. Ginger, *ACS Nano* **2014**, *8*, 10799.

[22] V. D. Mihailetchi, L. J. A. Koster, P. W. M. Blom, C. Melzer, B. de Boer, J. K. J. van Duren, R. A. J. Janssen, *Adv. Funct. Mater.* **2005**, *15*, 795.

[23] V. D. Mihailetchi, L. J. A. Koster, J. C. Hummelen, P. W. M. Blom, *Phys. Rev. Lett.* **2004**, 93.

[24] J. Shi, X. Xu, D. Li, Q. Meng, *Small* **2015**, *11*, 2472.

[25] L. Onsager, *J. Chem. Phys.* **1934**, 2.

[26] C. Sheng, C. Zhang, Y. Zhai, K. Mielczarek, W. Wang, W. Ma, A. Zakhidov, Z. V. Vardeny, *Phys. Rev. Lett.* **2015**, 114.

[27] V. D'Innocenzo, G. Grancini, M. J. P. Alcocer, A. R. S. Kandada, S. D. Stranks, M. M. Lee, G. Lanzani, H. J. Snaith, A. Petrozza, *Nat. Commun.* **2014**, 5.

[28] F. Deschler, M. Price, S. Pathak, L. E. Klintberg, D.-D. Jarausch, R. Higler, S. Huettner, T. Leijtens, S. D. Stranks, H. J. Snaith, M. Atatuere, R. T. Phillips, R. H. Friend, *J. Phys. Chem. Lett.* **2014**, *5*, 1421.

[29] a) W. Nie, H. Tsai, R. Asadpour, J.-C. Blancon, A. J. Neukirch, G. Gupta, J. J. Crochet, M. Chhowalla, S. Tretiak, M. A. Alam, H.-L. Wang, A. D. Mohite, *Science* **2015**, *347*, 522; b) A. Fakharuddin, F. Di Giacomo, A. L. Palma, F. Matteocci, I. Ahmed, S. Razza, A. D'Epifanio, S. Licoccia, J. Ismail, A. Di Carlo, T. M. Brown, R. Jose, *ACS Nano* **2015**, *9*, 8420.

[30] C. Xiangyu, D. Taguchi, T. Manaka, M. Iwamoto, *Appl. Phys. Lett.* **2014**, *104*, 013306.

[31] a) H. J. Snaith, A. Abate, J. M. Ball, G. E. Eperon, T. Leijtens, N. K. Noel, S. D. Stranks, J. T.-W. Wang, K. Wojciechowski, W. Zhang, *J. Phys. Chem. Lett.* **2014**, *5*, 1511; b) H.-S. Kim, N.-G. Park, *J. Phys. Chem. Lett.* **2014**, *5*, 2927.